Materials Science & Engineering A 798 (2020) 140074

Contents lists available at ScienceDirect

Materials Science & Engineering A

journal homepage: http://www.elsevier.com/locate/msea

In situ indentation and high cycle tapping deformation responses in a nanolaminate crystalline/amorphous metal composite

Qianying Guo [a,b], Yucong Gu [a], Christopher M. Barr [c], Thomas Koenig [a], Khalid Hattar [c], Lin Li [a], Gregory B. Thompson [a,*]

[a] *The University of Alabama, Department of Metallurgical & Materials Engineering, Tuscaloosa, AL, 35487, United States*
[b] *Oak Ridge National Laboratory, Oak Ridge, TN, 37831, United States*
[c] *Sandia National Laboratories, Albuquerque, NM, 87185, United States*

ARTICLE INFO

Keywords:
Multilayer
In situ TEM
Automated crystal orientation mapping
Crystalline/amorphous
Indentation
Cyclic loading

ABSTRACT

The incorporation of nanostructured and amorphous metals into modern applications is reliant on the understanding of deformation and failure modes in constrained conditions. To study this, a 105 nm crystalline Cu/160 nm amorphous $Cu_{45}Zr_{55}$ (at.%) multilayer structure was fabricated with the two crystalline layers sputter deposited between the top-middle-bottom amorphous layers and prepared to electron transparency. The multilayer was then *in situ* indented either under a single load to a depth of ~ 100 nm (max load of ~ 100 μN) or held at 20 μN and then repeatedly indented with an additional 5 μN up to 20,000 cycles in a transmission electron microscope to compare the deformation responses in the nanolaminate. For the single indentation test, the multilayer showed serrated load-displacement behavior upon initial indentation inductive of shear banding. At an indentation depth of ~ 32 nm, the multilayer exhibited perfect plastic behavior and no strain hardening. Both indented and fatigue-indented films revealed diffraction contrast changes with deformation. Subsequent Automated Crystal Orientation Mapping (ACOM) measurements confirmed and quantified global texture changes in the crystalline layers with specifically identified grains revealing rotation. Using a finite element model, the in-plane displacement vectors under the indent mapped conditions where ACOM determined grain rotation was observed, indicating the stress flow induced grain rotation. The single indented Cu layers also exhibited evidence of deformation induced grain growth, which was not evident in the fatigue-indented Cu based multilayer. Finally, the single indented multilayer retained a significant plastic crater in the upper most amorphous layer that directly contacted the indenter; a negligible crater impression in the same region was observed in the fatigued tested multilayer. These differences are explained by the different loading methods, applied load, and deformation mechanisms experienced in the multilayers.

1. Introduction

Metallic composites with nano-crystallites embedded within an amorphous metal matrix have found wide applicability in ball bearings, gears, and hard coatings because of their distinct mechanical properties [1,2]. The amorphous metals can exhibit a range of excellent physical properties including high strengths with large elastic responses [3,4], as well as good corrosion resistance [5]. However, these materials suffer from limited ductility associated with catastrophic failure from shear bands [6,7] that nucleate and create shear transition zones (STZs) [8–10]. The propagation of these shear bands in the amorphous materials is extremely fast, usually several millimeters per second [11], fracturing the material apart. One way to mitigate this rapid propagation is by inserting the crystalline phases within the amorphous matrix that blunt the shear band. To date, incorporating crystalline phases into the metallic glass can be accomplished through partial crystallization via heat treatments [12,13], mechanical alloying by ball milling [14,15], as well as a specific growth of each phase during processing, as in the case of thin film deposition [16]. Each of these methods yield a composite material has shown significant improvements of ductility when compared to just the pure amorphous phase.

With the continued development of two-phase crystalline and amorphous composites, there has been significant interest in understanding co-deformation mechanisms. Glassy materials deform by shear

* Corresponding author.
E-mail address: gthompson@eng.ua.edu (G.B. Thompson).

https://doi.org/10.1016/j.msea.2020.140074
Received 12 June 2020; Received in revised form 6 August 2020; Accepted 7 August 2020
Available online 19 August 2020

banding whereas crystalline materials nominally deform by dislocation propagation. How these two deformation modes operate at the crystalline/amorphous (C/A) interface, and in particular how strain and STZs in the amorphous layer induces elastic and plastic deformation in the crystalline layer, offers an area of fertile investigation. For example, molecular dynamics (MD) simulations have revealed that when plasticity flows from the crystalline into the amorphous phase, the dislocations (now impeded by the C/A interface) activate STZs [17–27]. These C/A interfaces as well as the amorphous layer itself are suspected to serve as a high-capacity sinks for dislocations.

To systematically study the deformation in C/A composites from an experimental perspective, multilayered thin films are ideal architectures because one can have a fixed surface area over the substrate while simply changing the thickness to precisely control the volume fraction [28–33]. By changing the individual layer thicknesses, the spacing between the phases is precisely controlled. In addition, by utilizing a multilayered stack, how deformation propagates through a periodically repeated C/A interfaces can easily be studied [34,35]. Prior MD simulations have even shown that by regulating the size of the amorphous layer, shear instability can be mitigated enabling a desirable combination of strength and ductility to be achieved in multilayered nanocomposites [19,20,27]. For those reasons, this paper will utilize a multilayered film of crystalline Cu/amorphous CuZr for such investigations.

Over the past decade, both *ex situ* and *in situ* mechanical tests have been performed on C/A multilayers with a variety of microstructural deformation responses reported. In particular, *in situ* nanomechanical platforms via scanning electron microscopy (SEM) or transmission electron microscopy (TEM) has allowed researchers, in real time, to observe how each of these phases deform [16,36]. Chou et al. [37] reported *in situ* SEM pillar compression of crystalline Ta/amorphous ZrCuTi multilayers where the amorphous layer thickness was fixed and the crystalline layer thickness was variable. Plastic flow was observed to be present at specific Ta layer thicknesses with shear banding hindered by the C/A interfaces. Later, Knorr et al. [38] reported both nanoindentation and pillar compression tests on crystalline Cu/amorphous PdSi multilayers. They too noted that the C/A interfaces appeared to improve strength and ductility of the composite by blocking dislocation propagation from the crystalline phase to the glassy phase. This, in turn, caused the Cu layer to deform heavily and be the primary phase to accommodate the deformation which reduced the stress concentration in the amorphous layers [38]. Similar phenomenon related to the C/A interfaces have also been observed in the crystalline Cu/amorphous CuZr multilayers. Here the dislocations propagate through the Cu layers and are absorbed at the C/A interfaces enabling 'self-toughening' to be achieved [34]. One of the most systematic studies in the Cu/CuZr systems was done where the Cu layer thickness varied to understand the effect of the crystalline phase's length scale on the collective deformation response [39]. In these *ex situ* nanoindentation and *in situ* SEM pillar compression tests, three main deformation responses were observed. They are the following: (1) When the Cu layers were thin (~5 nm), shear banding dominant deformation was noted with the shear bands propagating through both phases; (2) When the Cu layer thickness was ~ 20 nm, plastic co-deformation in the two phases was observed. And (3) dislocation dominant mechanisms were seen in the thicker Cu (~100 nm) layered multilayers [39]. This type of deformation mechanism transition has also been discussed by other researchers with all of these modifications attributed to the C/A interfaces [40,41]. Though these types of studies are paramount in understanding the specific mechanical responses and 'global nanoscale' deformation behaviors in the material, the limited resolution of *in situ* SEM images, with the simultaneous loading, inhibits a closer inspection of the localized nanoscale deformation mechanisms that operate. This information is bridged through similar studies using *in situ* TEM.

In recent years, Precession Electron Diffraction (PED) enhanced Automated Crystal Orientation Mapping (ACOM) in the TEM has developed as an approach to provide quantitative information on grain boundary misorientation, texture, grain size, and phase identification. By using ACOM in the TEM, one is able to achieve much higher spatial resolutions (~1-3 nm) than analogous imaging techniques such as electron backscattered diffraction, EBSD, (~ 50-100 nm) in the SEM [42–53]. By precessing the electron beam, a pseudo-kinematical diffraction condition is achieved which reduces intensity variations in the diffraction spots as well as enabling more of reciprocal space to be captured increasing the number of spots collected. This collectively improves the reliability index in identifying the crystalline phase's diffraction pattern. By serially moving the precessed probe, and collecting the diffraction patterns at each location, changes in grain texture are quantitatively observed enabling indexing for a reconstructed map of grain orientations. The use of ACOM has helped bridge experimental *in situ* deformation works in the TEM with molecular dynamics simulations [20,21].

All of these previous studies on nanocrystalline-amorphous nanolaminate behavior and their associated deformation mechanisms done under monotonic loading states. There have been far fewer investigations into cyclic loading of such composites, and of those types of studies, they were done using partially crystallized bulk composite structures [54–56]. To the authors' knowledge, there have not been any similar cyclic studies using nanolaminate structures. These types of investigations would enable a better understanding of how these composites would deform in their potential use as components and/or coatings where repeated contact occurs such as application in gear based machinery.

In this paper, we aim to extend these previous *in situ* TEM deformation studies of C/A multilayers by applying both monotonic and cyclic indent loading (tapping) and quantifying how the crystalline grain orientation, size, as well as texture evolve under these type of deformation conditions. This will be achieved by correlating *in situ* TEM indentation/fatigue and the ACOM technique using the crystalline Cu/amorphous CuZr multilayers as the case study. As reported in other works [40,57], with different loading conditions, the multilayer will have different deformation mechanisms. By coupling bright field TEM, ACOM analysis on the same pre- and post-test areas with detailed finite element modeling, we will be able to understand how the nanolaminate, especially the crystalline grains respond to the deformation.

2. Experimental and computational modeling procedure

Nanocrystalline Cu (2 layers)/amorphous $Cu_{45}Zr_{55}$ (at.%, 3 layers) multilayer was sputter-deposited onto the edge of pre-fabricated Si wedge [58] that has been micro-machined and etched for the purpose of readily producing an electron transparent film for indentation and fatigue studies. The multilayer was grown in an AJA ATC-1600 sputtering chamber from a $Cu_{45}Zr_{55}$ (at.%) alloyed target and an elemental Cu target. The amorphous $Cu_{45}Zr_{55}$ layer thickness was fixed at 160 nm, and would be the bottom layer (initial growth) as well as the final top layer in the stack. The Cu layers, grown to a thickness of 105 nm each, were placed in between the 3 amorphous layers. The pressure of the sputtering chamber was $<1.33 \times 10^{-6}$ Pa prior to sputtering and kept at 0.133 Pa during sputtering with the working gas being ultrahigh purity argon flowed into the chamber at a rate of 0.01 L/min. The multilayer was deposited at room temperature (~ 23 °C).

To further improve the electron transparency of the film on the wedge, several 10 μm in width × ~1 μm in height and <100 nm in thickness regions were focus ion beam (FIB) milled parallel to the wedge surface from the top of the film into a portion of the Si wedge. This ensured the film was uniform in thickness for imaging and indention. This milling was done in a Tescan Lyra 3XM dual SEM-FIB following the TEM cross-section sample thinning technique given in Ref. [59–61]. The initial thinning was done at 30 keV with a width of ~10 μm with step down ion currents from 0.2 nA to 0.03 nA. A subsequent low keV clean-up at 5 keV at a beam current of 20 pA was done to remove any surface damage created by the Ga^+ implantation into the sidewalls of the foils [62]. The Si wedge was then mounted into in the designed Bruker (formally Hysitron) PI95 Pico-indenter TEM sample stage holder using conductive silver epoxy for the *in situ* mechanical tests.

The *in situ* mechanical loading was carried out in this PI95 PicoIndenter, which provides quantitative load and displacement data. The holder, with foil, was inserted inside an FEI Tecnai G^2 F20 Super-twin (Scanning) Transmission Electron Microscope ((S)TEM) operated at 200 keV fitted with a NanoMEGAS© ASTAR PED-ACOM orientation identification platform. The precession angle used for analysis was 0.1° at step sizes of 2 nm [63]. The ACOM scans were performed on the tested area pre- and post-deformation to capture the microstructural change from the test with the indentation or fatigue being from a cube corner diamond tip controlled by piezo-motor and Micro-Electro-Mechanical Systems (MEMS) based transducer in the PI95. In some cases, the TEM diffraction patterns, acquired by the ASTAR platform, were not indexed because of intrinsic ambiguities associated with either low Bragg angles and/or the lack of a high order Laue Zone. As a result, the standard procedure of automatic indexing of these diffraction patterns is not achieved and are devoid (black) in the reconstruction. Furthermore, other diffraction issues include ambiguities, especially the so-called 180° ambiguity [64] where grain boundaries are factiously assigned. In those cases, the 180° ambiguity was corrected by using the Ambiguity Resolver function in the MapViewer V2 software purchased from NanoMEGAS©. Specifically, the degree of ambiguity is weighted by the ambiguity parameter *R*, defined as

$$R = 100 \times \left(1 - \frac{I_2}{I_1}\right) \tag{1}$$

where I_1 and I_2 are the correlation index of the best match and the 180° rotated diffraction templates [65]. A detected lower *R* value indicates a higher possibility of suffering 180° ambiguity. The solution with low *R* values is then exchanged to one with a 180° rotation around the zone axis. By making this comparison, one can remove the majority of the 180° ambiguity in the ACOM reconstructed data [66] and was successfully applied to the research performed here.

In all cases, the reconstructed ACOM grains were compared to bright field TEM images from the equivalent regions to further increase our confidence in the reconstructions, particularly the size and shape of the grains. Post-analysis of ACOM data sets for grain size and misorientation were performed off-line using the TSL OIM Analysis 7 software platform. A set of conservative clean-up values with a grain tolerance angle of 5°, minimum grain size of 10 nm, and neighbor confidence interval correlation value of 0.05 were chosen as the data processing parameters to avoid possible smoothing artifacts [67]. The reconstructed ACOM results were compared to bright field images of the same regions to ensure accuracy in the identified grains via size and shape. To further ensure the reliability of the ACOM data and remove any potential sample thickness induced diffraction overlapping artifacts, two filters were applied during post analysis, which are filters for allowing only grain sizes ≥10 nm to be mapped at a confidence index (CI) ≥ 0.1. If the grains did not meet this criteria, they were not indexed and will appear and are also 'blacked-out' regions in the ACOM map.

The *in situ* TEM nanoindentation experiment was carried out under a displacement control mode with a constant rate of 1 nm/s until the overall displacement reached 105 nm. Then unloading was performed at a speed of 1 nm/s until the start point was reached. Cyclic loading test was carried out under a load control mode with a mean load at 20 μN and a load amplitude equal to 5 μN. As will be shown in the monotonic loading, this cyclic load condition was in the elastic/micro-plastic region for our composite and is why it was selected, i.e. to avoid plastic deformation and ascertain if and how repeated elastic responses evolved the nanostructure. The cyclic loading frequency was 20 Hz and total loading time of 1000 s or an overall application of 20,000 cycles.

It is noted that the alignment of the tip and the specimen can be difficult but is a common challenge to any similar *in situ* indentation TEM study. For the indentation test, we used a cube corner tip that was rounded (or blunt) with an estimated radius of curvature of 540 nm. Here the indenter's radius of curvature is more than the thickness of the foil. The bluntness ensures the tip-specimen indentation contact reduces the side contact conditions. In the case of the cyclic fatigue test, the indenter tip used was more pronounced with a radius of curvature of 170 nm. As would be expected with any high cycle indenting test, particularly one where the indent is into a thin foil, some drift is expected. When this issue was noted in our experiment, the tip was re-aligned.

To further quantitatively analyze the deformation process, a finite element (FE) model was established based on the *in situ* indentation process of $Cu/Cu_{45}Zr_{55}$ multilayer geometry in the TEM, including indenter shape and properties, multilayer geometric dimensions, and the substrate with an overall FIB window size of $6 \times 2\ \mu m^2$. The details of the FE model is found in the supplementary section of this paper, i.e. Figs. S1–S6. Both the indenter and entire sample-substrate region were heavily meshed (with a total of 1,770,120 elements) with the bottom of the substrate fixed. As a result, this bottom surface will have no movement and rotation in any direction during the simulation. The indenter was also fixed and can only move perpendicular into the multilayer to simulate the indentation process. Finally, each layer is bonded to the layer underneath it, and the bottom amorphous layer is bonded to the Si wedge to ensure no small slide or separation.

3. Experimental results

3.1. Indentation deformation

Fig. 1 is the load-displacement curve during the nanoindentation experiment with selected TEM bright field images at specific loads for this multilayer. Fig. 1(a) shows the load-displacement curve for the $Cu/Cu_{45}Zr_{55}$ multilayer under indentation and five selected loads, (b) – (f), are marked on this curve. This curve reveals a linear response and nearly perfect flattened response upon loading for this multilayer. A small shift in the slope is observed (circled) on this loading curve and is believed to be evidence of the first pop-in event that corresponds to a shear banding event in the amorphous layer [3,68]. Such a yield point deformation was located at an indentation depth of ~ 17 nm. However, the clear transition in the slope was near an indentation depth of ~ 32 nm. The TEM bright field images at this state did not readily reveal a clear enough image of shear band(s) propagated in the multilayer; though the mechanical response in the load vs. displacement would suggest that such an event did occur by the 'pop-in' displacement in Fig. 1(a). After greater penetration depths, the loading maintained a relatively constant value near 103 μN to a final displacement of 105 nm.

With the mechanical property responses reported, we now link these to the structure of the multilayer. Three specific grains, marked from #1 to #3, are shown throughout Fig. 1(b)–(g), allowing us to track how the deformation proceeds through the multilayer via their contrast change. Fig. 1(b) is the zero-load condition. The darker layers are the amorphous (A) layers and the brighter contrast are nanocrystalline (C) Cu layers. In Fig. 1(b), grains #1 and #2 are relatively smaller grains as compared to grain #3. We would also like to highlight the very narrow shaped grain (evident by the dark contrast band) that is observed inside the coarser grain #3. When the load reached the end of the linear portion, point (c), the contrast of some of these grains have clearly changed, including grain #1, which become brighter, as shown in Fig. 1(c). This indicates that the load transfer was occurring in both Cu layers (one closest and one furthest from the indent impression). Other contrast changes can be noted in other grains in both Cu layers by comparing Figs. 1(b)–2(c). The change in grain contrast indicates potential grain rotation [69] in response to the deformation as the grains come in and out of Bragg scattering. This will be expanded upon with the forthcoming ACOM data. Though not all grains appear to show a noticeable contrast change,

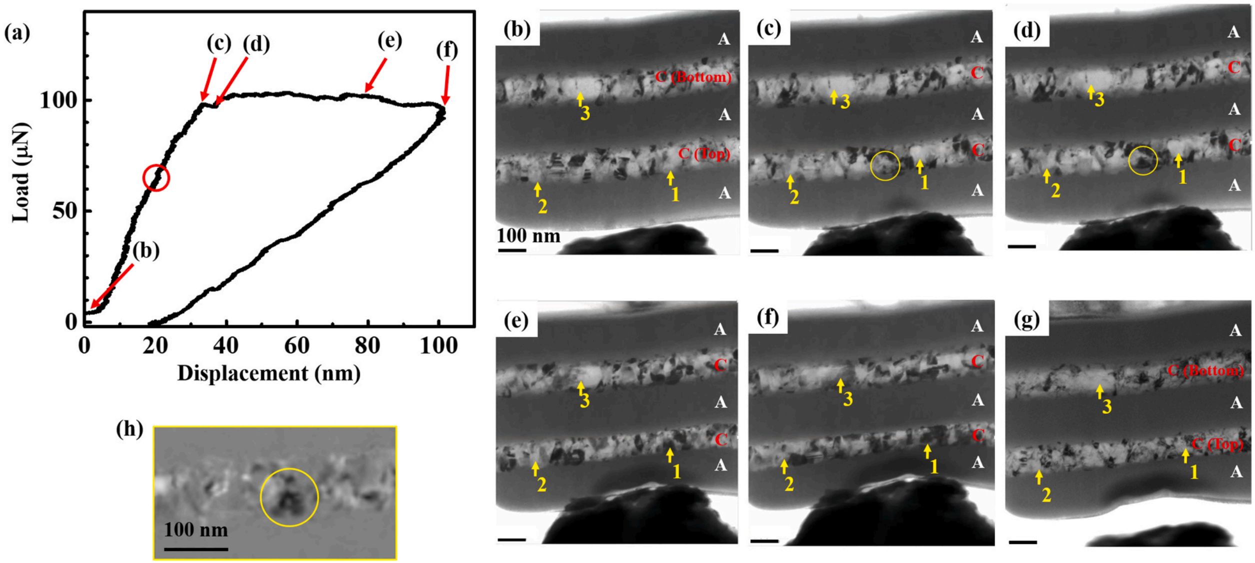

Fig. 1. (a) Load-displacement curves of Cu 105 nm/$Cu_{45}Zr_{55}$ 160 nm multilayer during indentation test. 'A' represents the amorphous phase and 'C' the crystalline phase. Five points are selected on the curve with the corresponding TEM bright field images shown from (b) to (f). **(b)** TEM bright field image at point (b) on the curve. **(c)** TEM bright field image at point (c) on the curve. **(d)** TEM bright field image at point (d) on the curve. **(e)** TEM bright field image at point (e) on the curve. **(f)** TEM bright field image at point (f) on the curve. **(g)** TEM bright field image at ~ 0 nm displacement after unloading. **(h)** Magnified difference image between the rectangular regions in (c) and (d) and circled darker region indicates the difference.

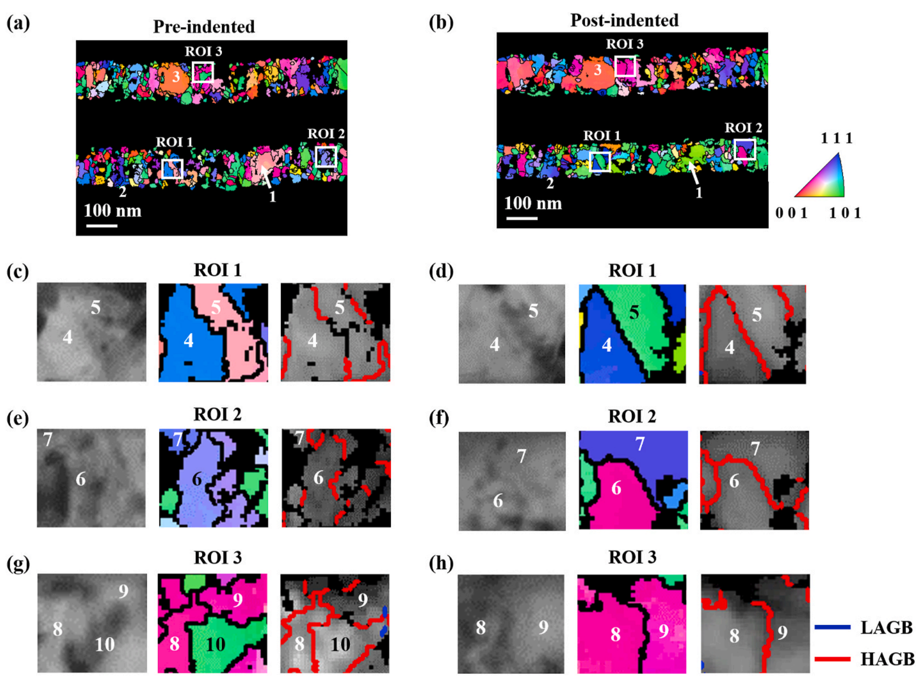

Fig. 2. (a) Grain orientation map of Cu 105 nm/$Cu_{45}Zr_{55}$ 160 nm multilayer pre-indented with three grains and three ROIs selected. **(b)** Grain orientation map of Cu 105 nm/$Cu_{45}Zr_{55}$ 160 nm multilayer post-indented with three grains and three ROIs selected. **(c)** Magnified bright field TEM image (left), grain orientation map (middle) and IQ map (right) of pre-indented ROI 1. **(d)** Magnified bright field TEM image (left), grain orientation map (middle) and IQ map (right) of post-indented ROI 1. **(e)** Magnified bright field TEM image (left), grain orientation map (middle) and IQ map (right) of pre-indented ROI 2. **(f)** Magnified bright field TEM image (left), grain orientation map (middle) and IQ map (right) of post-indented ROI 2. **(g)** Magnified bright field TEM image (left), grain orientation map (middle) and IQ map (right) of pre-indented ROI 3. **(h)** Magnified bright field TEM image (left), grain orientation map (middle) and IQ map (right) of post-indented ROI 3. In IQ maps, red grain boundaries are HAGBs with misorientation $>15^\circ$ and blue grain boundaries are LAGBs with misorientation $\leq 15^\circ$. Color available online. (For interpretation of the references to color in this figure legend, the reader is referred to the Web version of this article.)

i.e., grains #2 and #3. This indicates that the deformation responses are localized to specific regions in the film at this load state. After point (c) in Fig. 1(a), the load drops slightly when the displacement continues to increase for approximately 2 nm or point (d). By comparing Fig. 1(c) and (d), the only notable contrast change the authors observed was that in the circled region, it comes increasingly darker and is symmetrically located directly under the indent. This change is magnified by the overlapping and pixel subtracting images of (c) and (d) in Fig. 1(h).

Further increasing displacement to 78 nm, point (e), much more pronounced contrast changes are observed throughout the crystalline layers as well as a notable semi-circle of contrast in the amorphous layer that is in direct contact with the indenter, Fig. 1(e). In this same figure, the contrast change of grain #1 from the previous light grey is now strongly diffracting or black. Negligible to only slight contrast changes were detected in grain #2. The very narrow grain previously presented in grain #3 is now barely observable in Fig. 1(e) suggesting that it has been consumed from some form of grain boundary migration [67, 70–72]. Fig. 1(f) is the multilayer at the maximum displacement of 105 nm. The contrast of the indented area is clearly present throughout the entirety of the uppermost amorphous film that is in contact with the indenter. Grains #1 and #3 are even darker consistent with a strongly diffracting condition with grain #2 being the notable exception, which appears to have kept a relatively invariant contrast throughout the loading experiment. Such contrast preservation indicates negligible grain orientation disruption during nanoindentation, which again will be further proven in the ACOM data.

After unloading, the indentation-induced contrast in the first contacted amorphous layer remained, Fig. 1(g), with a plastic crater impression. This crater impression is further supported by the ~ 18 nm difference in retraction distance back to the original origin where a 0 μN load is recorded during the unloading curve in Fig. 1(a). (Recall from the experimental section, the displacement is a measure of the indenter travel.) Besides the crater, a thickness change is also noted at the center portion of the top Cu layer, from ~ 68 nm in thickness where the maximum indent contact depth occurred, Fig. 1(f), to a recovered thickness of ~ 79 nm when the indenter is removed from the foil, Fig. 1(g). Further note that grains #1 and #3 have now became brighter while grain #2 still retained its prior contrast after unloading, Fig. 1(g). Of all the grains specifically identified, arguably grain #3 revealed the most contrast change under the entirety of the indentation process. It appears that this grain has undergone growth, but the dynamical diffraction contrast in the TEM bright field image hinders a conclusive determination of its boundary locations and motivates the use of ACOM in these types of studies.

The ACOM scans were performed for the $Cu/Cu_{45}Zr_{55}$ multilayer in the pre- and post-indentation states with the orientation mapping of the Cu layers shown in Fig. 2. Fig. 2(a) and (b) are the grain orientation maps that clearly delineate the grains by the multitude of textures evident in the grain colors and the black lines showing the grain boundary locations. We should note that some of the dark areas were observed in the Cu layers, which are low reliability regions meshed off after applying the grain size and confidence index filters described in the experimental section. Each of the grains in Fig. 1 are now specifically labeled in Fig. 2(a) and (b). In addition, three region of interests (ROIs) were selected and marked on Fig. 2(a) and (b).

Before indentation, grain #1 has a ~ {113} orientation (8.5° from this orientation); after indentation, it has evolved to a {101} orientation. Its relative shape is intact but appears rotated clockwise by 16.8°. Since orientation is described by plane and direction, we have provided in the supplementary section of this paper the full lattice orientation description for this grain and all others specifically identified in Fig. 2. Nevertheless, in the current representation shown in Fig. 2, the orientations reveal the quantitative evolution that has been undergone in the crystalline layer from the loading process. Unlike grain #1, grain #2's ACOM data indicates that it retained its general triangular shape and a near {111} texture pre- and post-testing, indicating the foil has not undergone macroscopic bending to create these texture changes. This is further confirmed by the retention of the large grain #3 in Fig. 2 in the pre- and post-indent condition. This ACOM result for grain #2 would be consistent with the prior comments that it lacked diffraction contrast changes in the bright field images of Fig. 1.

Besides grain rotation (or no rotation), grain growth was also observed. If one looks at the Cu layer closest to the indent and directly under the indent, it is difficult to make a direct link to which grains map

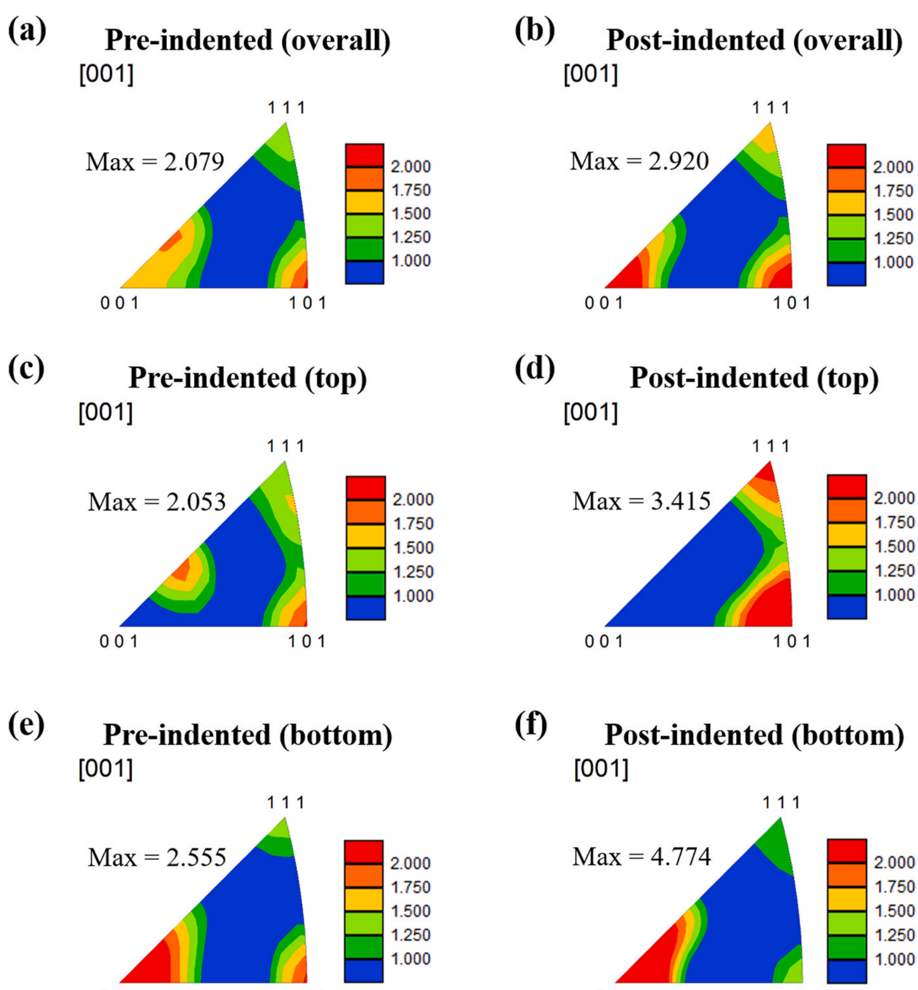

Fig. 3. IPF texture maps of **(a)** overall Cu layers pre-indented **(b)** overall Cu layers post-indented **(c)** top Cu layer pre-indented **(d)** top Cu layer post-indented **(e)** bottom Cu layer pre-indented **(f)** bottom Cu layer post-indented in Cu 105 nm/$Cu_{45}Zr_{55}$ 160 nm multilayer. Color available online. (For interpretation of the references to color in this figure legend, the reader is referred to the Web version of this article.)

to each other. Nevertheless, the textures are different and even the relative grain sizes appear larger. The average gain size (of the same region) in the pre- and post-condition will be discussed in the following Fig. 4. Specifically identifying grain #3, the grain growth is readily mapped. In grain #3, the orientation under indentation was relatively invariant at ~ {103}. However, the prior to indentation, a narrow grain, delineated by the green color {101} and black boundaries can be seen to the left of grain #3 in Fig. 2(a). After indentation, this small 'green grain' is consumed by grain #3, Fig. 2(b). Even the pink hue grain {112} to the left of the smaller green {101} grain appears to have also been consumed by grain #3 after indentation. This collectively confirms deformation induced grain growth [73,74].

To further confirm grain growth and grain rotation, three ROIs were selected on the orientation maps in Fig. 2(a) and (b) and the correlated magnified grain orientation maps (left) and image quality (IQ) maps with grain boundary information, Fig. 2(c)–(h). Fig. 2(c) and (d) are the magnified orientation and IQ maps of ROI 1 before and after indentation. In the IQ maps, the red grain boundaries are high angle grain boundaries (HAGBs) and are defined with a misorientation $> 15^{\circ}$. The blue boundaries are low angle grain boundaries (LAGBs) with a misorientation $\leq 15^{\circ}$. Grains #4 and #5, in Fig. 2(c), are identified with a {111} and ~ {112} orientation, respectively, pre-indented. In addition, a HAGB lays between these two grains. After indentation, grain #4 maintained the {111} orientation while grain #5 rotated to a {101} orientation, Fig. 2(d), which is about a 30° rotation and the HAGB is retained. Again, the invariance of one grain's orientation after indentation while another grain changes its orientation (that is directly next to it) confirms that grain rotation is an active deformation mechanism and not a rigid boundary rotation of the TEM foil. Clearly, ACOM improves the clarity to confirm these types of observations that is often confounded in interpreting simple contrast changes in traditional bright field images.

The details of ROI 2 are shown in Fig. 2(e) and (f). Before indentation, grains #6 and #7 existed similar ~ {111} orientation with HAGBs, Fig. 2(e). The results of post-indented maps reveal a clear orientation change in grain #6, to a {112} orientation, while limited orientation changes detected in grain #7, Fig. 2(f). Moreover, grain growth is noted in grains #6 and #7 when comparing pre- and post-indented maps.

Inside ROI 3, grains #8, #9, and #10 were marked in Fig. 2(g). Grain #8 and #9 had a ~ {112} orientation and grain #10 had a {101} orientation. The grain boundaries between them are all HAGBs. After indentation, grain #10 was consumed by grains #8 and #9, with a HAGB separating them, which is additional evidence of deformation induced grain growth. Moreover, this grain growth also supports how the texture evolves in the nanolaminate beyond just grain rotation. The prior #10 {101} orientation was lost by its consumption of #8 and #9 being {112}. All the detailed analysis of these ROIs indicates a combined grain rotation and grain growth mechanisms in these nanocrystalline Cu layers with two free surfaces during indentation.

The following texture analysis of the pre- and post-indented Cu layers, based on the ACOM data, is shown by the inverse pole figure in Fig. 3. In the supplementary section of this paper, the specific pole figures for each orientation for each location in the composite is provided. Fig. 3(a) and (b) reveals the overall inverse pole figure (IPF) texture plot of the scanned area (Cu layers) pre- and post-indentation. The pre-indent Cu layers have a relatively strong {001}-{112} and {101} texture with minor {111} textures, Fig. 3(a). Here the texture orientation is normal to the orientation images of the grains in Fig. 2(a) and (b). After indentation, the {101} is still retained but the previous {001}-{112} texture changed, with a reduction of the {112} texture and the relative stronger {001} texture. Furthermore, the prior minor {111} texture has developed an increase in texture presence. The texture analysis of the individual Cu layers pre- and post-indentation are plotted in Fig. 3(c)–(f). Here, we define the Cu regions closer to the indenter Cu layer (top layer) and further from the indenter (bottom layer). Fig. 3(c) and (d) are the IPF texture maps of the top Cu layer pre- and post-indented. Similarly to the overall texture, the texture evolution in the top Cu layer increases in the {111} and {101} texture and a disappearance of {112} texture during indentation. The only difference is that the {001} texture was not detected in the top layer both before and after indentation. The texture maps of the bottom Cu layers before and after indentation are plotted in Fig. 3(e) and (f), and orientation changes are not as obvious, though a slightly stronger {111} and weaker {101} texture is detected between the two loading conditions for the bottom layer. These 'more global' texture changes further prove a collective grain rotation in the sample as a deformation mechanism, especially in the top Cu layer.

The grain size distribution, determined by ACOM, is plotted in Fig. 4 in the pre- and post-indent conditions. The area fraction vs. grain size plot of the overall Cu phase (top and bottom layers) is shown in Fig. 4(a), with the solid bar for the pre-indented data and dashed bar for the post-indented data. The average grain size of the Cu grains in both layers is 34 ± 10 nm (pre-indented) and 45 ± 13 nm (post-indented). The largest grain among all the Cu grains is 93 nm before indentation and increased to 122 nm after indentation. Combined with the previous orientation maps in Fig. 2, this largest grain is grain #3. Similar grain size analysis for the individual top and bottom Cu layers and is plotted in Fig. 4(b) and (c) for top and bottom layer, respectively. In the top layer, the overall Cu grain size is 29 ± 9 nm (pre-indented) and 31 ± 10 nm (post-indented), indicating a relatively limited amount of deformation induced grain growth. A notable example is seen in the top layer for grains #6 and #7 in ROI 2 in Fig. 2. For the bottom layer, its average grain size evolved from 39 ± 11 nm to 56 ± 16 nm, indicating grain growth. Indeed, the largest grain was detected in this layer, i.e. grain #3, which consumed the surrounding smaller grains during indentation. The grains in the bottom Cu layer grew more as compared to the top layer, Fig. 3, but the top layer appears to experience more pronounced grain rotation, Fig. 3.

3.2. High cycle fatigue deformation

A fatigue test was then applied on the same type of multilayer structure but now on a different FIB milled window. Fig. 5 are the TEM bright field images of the 105 nm Cu/160 nm $Cu_{45}Zr_{55}$ nanolaminate taken before, during, and after cyclic loading with some specific Cu grains (labeled numbers #1 to #7) marked inside three different ROI's (numbered 1 to 3) in both Cu layers. Each ROI contains three

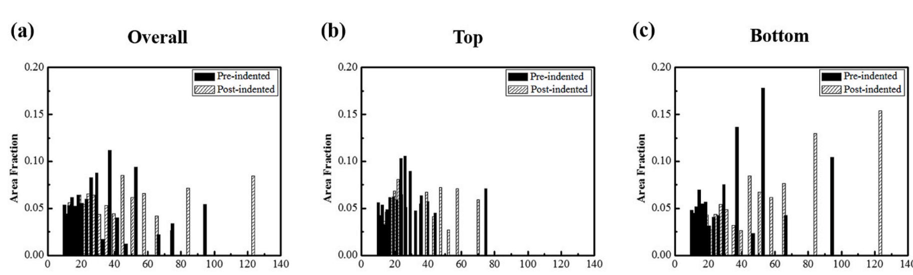

Fig. 4. The pre- and post-indented grain size histogram of **(a)** overall Cu layers **(b)** top Cu layer **(c)** bottom Cu layer.

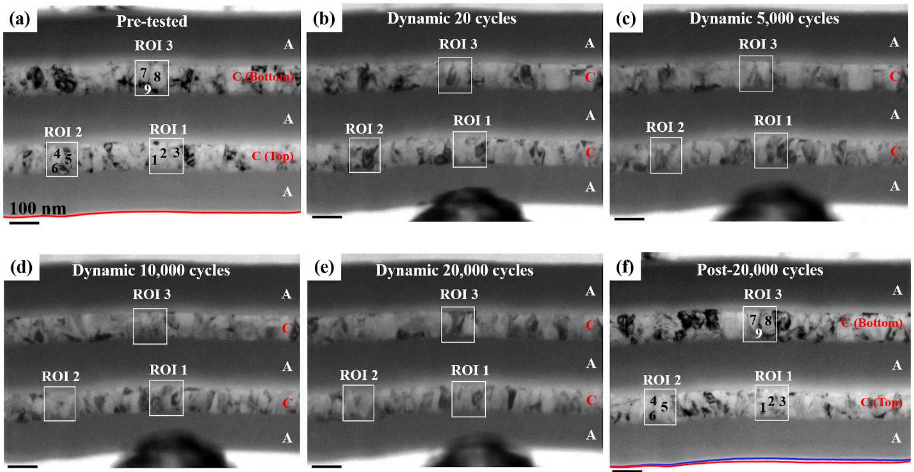

Fig. 5. Selected bright field TEM images of Cu 105 nm/$Cu_{45}Zr_{55}$ 160 nm multilayer at **(a)** pre-tested condition **(b)** dynamic 20 cycles **(c)** dynamic 5000 cycles **(d)** dynamic 10,000 cycles **(e)** dynamic 20,000 cycles **(f)** post 20,000 cycles conditions. 'A' represents the amorphous phase and 'C' the crystalline phase. Red line and blue line were drawn at the edge of the multilayer free surface at pre-tested and post-tested conditions in (a) and (f). (For interpretation of the references to color in this figure legend, the reader is referred to the Web version of this article.)

representative grains. ROI 1 is the Cu region directly under the loading area and the top Cu layer in the stack closest to the initial indent. ROI 2 are Cu regions in the same top Cu layer but on the left side of ROI 1. ROI 3 lays approximately above ROI 1 but in the bottom Cu layer. The TEM bright field image before the cyclic load is shown in Fig. 5(a). Three grains (#1, #2, #3) are marked in ROI 1 and the contrast of these three grains are generally bright (not in a strongly diffracting condition). Three other grains (#4, #5, #6) are marked in ROI 2. The contrast of grain #4 is bright whereas grains #5 and #6 were dark. Grains #7, #8, and #9 are detected in ROI 3. Two of them are bright (grain #7 and #8) with a narrow grain (#9) laying in between these two grains, being dark or in a strongly diffracting orientation. A red line has been included at the edge of the multilayer-free surface and will be further used to analyze plastic deformation after cyclic loading.

After 20 cycles of loading, the experiment was stopped and the resulting microstructure was again imaged and shown in Fig. 5(b). Comparing with Fig. 5(a), the qualitative contrast of the grains in ROI 1 became darker, especially for grain #3. In ROI 2, the grain contrast has noticeably changed, particularly grain #5 becoming much darker. In ROI 3, part of the shape of grain #9 (in between grain #7 and #8) appears to have changed and is now larger and darker, which might indicate a rotation and growth of grain #9 or a formation of (sub) structure between grain #7 and #8 changing its local orientation (diffraction) condition [57,75].

With increased fatigue cycles from 20 to 5,000, a continuous evolution of the microstructure in the three ROIs is apparent, Fig. 5(c) vs. Fig. 5(a) and (b). When comparing Fig. 5(c) with Fig. 5(b), grain #2 became darker in ROI 1. In ROI 2, it is hard to distinguish grain #4, #5, and #6 from the grey contrast region. The previous bright grain #4 region seems to be moving to the top center in ROI 2, and the previous darker grain #5 region became brighter and exhibited similar contrast to grain #6 in the same region. In ROI 3, grain #9 now has a distinct triangular shape clearly dividing grains #7 and #8.

Further increasing the loading cycles to 10,000, Fig. 5(d), more notable microstructure changes are observed. The contrast of grain #1 in ROI 1 is now grey, with all three grains in this ROI diffracting. The contrast continued to evolve for grain #4 to #5 in ROI 2 and the triangular shape of grain #9 in ROI 3 has widened to be more trapezoidal in shape between grains #7 and #8. When the cyclic loading increased to the 20,000 cycles, Fig. 5(e), the contrast of grains #1 and #2 in ROI 1 is reduced relative to 10,000 cycles. In ROI 2, we now have lost track of grain #4 to #6, while the triangle shaped contrast in the previous grain #4 and #5 regions is now observed. Grain #9 in ROI 3 has penetrated fully between grains #7 and #8 and has a 'dog-bone' shape. With the cyclic loading complete, and the indenter removed, Fig. 5(f) is the corresponding TEM bright field image. The contrast of the grains in ROI 1 are now bright. Grain #4 to #6 in ROI 2 appear again, with different contrasts to that of grain #5 and #6. Interestingly, grain #9 in ROI 3 is now reduced in size. In this same image, the edge of the multilayer after fatigue testing is marked by a blue line. By overlapping the previous undeformed multilayer's edge, the red line in Fig. 5(a), a very modest plastic crater of deformation is evident in the uppermost amorphous layer of the multilayer at the free surface. This indicates that some amount of plastic deformation has occurred during cyclic loading.

Overall observations from Fig. 5 includes clear contrast/shape changes for selected grains during cycling, with the contrast and shapes dependent on the number of cycles. This would suggest that grain rotation/grain shifting, dislocation accumulation and similar associated mechanisms were active. Though the bright field images are useful, they do not necessarily provide the clearest discernment of the evolution. To complement the bright field images, a series of corresponding ACOM scans of the pre- (0 cycles) and post-loading (20,000 cycles) was completed, as we did for the single indent experiment, and are shown in Fig. 6.

Fig. 6's ACOM scans were performed on the same area as the specific grains (#1 to #9) and ROIs (1–3) in Fig. 5. Fig. 6(a) and (b) are the grain orientation maps of the Cu layers pre- and post-cyclic loading. The previous selected ROI 1, 2, and 3 are marked on each grain orientation map. From these images, grain orientation changes are clearly apparent but also the grain shapes are delineated from each other. In Fig. 6(c) and (d), the magnified grain orientation map (left) and image quality (IQ) map with grain boundary lines overlaid (right) of ROI 1 before and after fatigue testing is shown. The red grain boundaries are HAGBs and are defined with a misorientation $>15°$. The blue boundaries are LAGBs with a misorientation $\leq 15°$. In Fig. 6(c), grains #1, #2 and #3 exhibit a near {212}, {105}, and {111} orientation, respectively. After the cyclic loading, grains 1 and 2 were rotated to a near {101} and {301} orientation while grain 3 retained the same {111} orientation, providing a reference that indeed individual grains are changing rather than a global bending of the foil. Upon closer investigation, the black regions near grains #1 to #3 are low reliability grains meshed off by applying the grain size and CI filter. Most of the grain boundaries in ROI in pre- and post-loading are HAGBs.

In Fig. 6(e), grains #4, #5 and #6 are from ROI 2 with the grain orientation map (left) and IQ map (right) and the grain boundary types overlaid. Grain #4 has an orientation near {121} while grains #6 and #5 are near {101}. Similar to ROI 1, most of the grain boundaries of grains #4, #5, and #6 are HAGBs. Fig. 6(f) shows the grain orientation map and IQ maps of ROI 2 after cyclic loading. Grains #4, #5 and #6 have now appeared to maintain their own shape and orientation. Grain growth occurred in grains #4 and #5 while grain #6's size decreased. In addition, most of the grain boundaries retained their HAGB structure

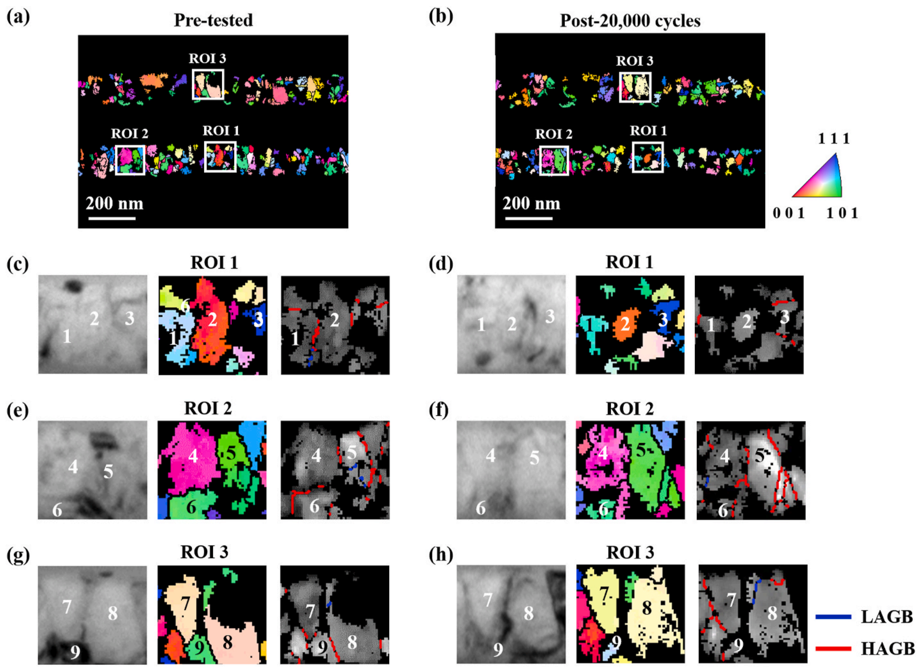

Fig. 6. (a) Grain orientation map of Cu 105 nm/$Cu_{45}Zr_{55}$ 160 nm multilayer pre-tested with three ROIs selected. **(b)** Grain orientation map of Cu 105 nm/$Cu_{45}Zr_{55}$ 160 nm multilayer post-tested with three ROIs selected. **(c)** Magnified bright field TEM image (left), grain orientation map (middle) and IQ map (right) of pre-tested ROI 1. **(d)** Magnified bright field TEM image (left), grain orientation map (middle) and IQ map (right) of post-tested ROI 1. **(e)** Magnified bright field TEM image (left), grain orientation map (middle) and IQ map (right) of pre-tested ROI 2. **(f)** Magnified bright field TEM image (left), grain orientation map (middle) and IQ map (right) of post-tested ROI 2. **(g)** Magnified bright field TEM image (left), grain orientation map (middle) and IQ map (right) of pre-tested ROI 3. **(h)** Magnified bright field TEM image (left), grain orientation map (middle) and IQ map (right) of post-tested ROI 3. In IQ maps, red grain boundaries are HAGBs with misorientation >15° and blue grain boundaries are LAGBs with misorientation ≤15°. Color available online. (For interpretation of the references to color in this figure legend, the reader is referred to the Web version of this article.)

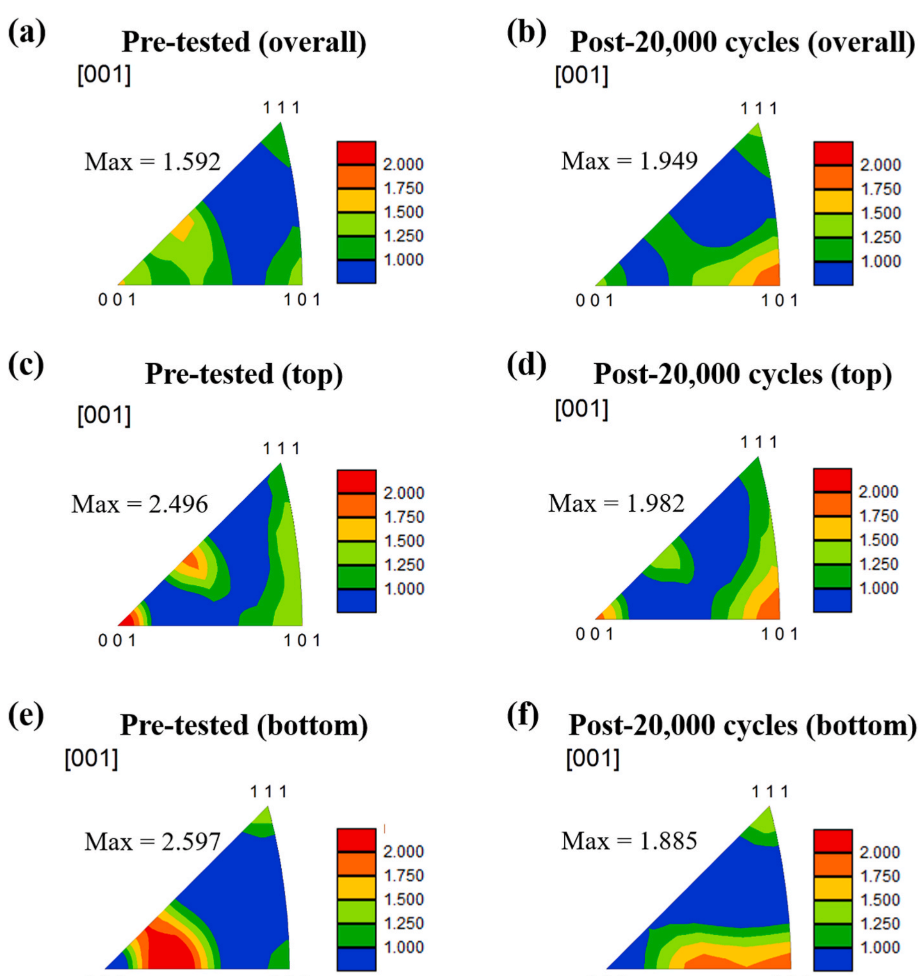

Fig. 7. IPF texture maps of **(a)** overall Cu layers pre-tested **(b)** overall Cu layers post-20,000 cycles **(c)** top Cu layer pre-tested **(d)** top Cu layer post-20,000 cycles **(e)** bottom Cu layer pre-tested **(f)** bottom Cu layer post-20,000 cycles in Cu 105 nm/$Cu_{45}Zr_{55}$ 160 nm multilayer. Color available online. (For interpretation of the references to color in this figure legend, the reader is referred to the Web version of this article.)

after cyclic loading.

Fig. 6(g) and (h) are the grain orientation and IQ maps of ROI 3 pre- and post-fatigue testing. In Fig. 6(g), grains #7 and #8 are two relatively large grains with a near {315} orientation. They were separated by 'dog bone' shaped {101} oriented gain labeled as #9. The grain boundaries between grains #7/#9 and grains #8/#9 are HAGBs. After cyclic loading, grains #7 and #8 appears to have maintained the original {315} orientation with $<10^{\circ}$ rotation between them. The size of grain #8 increased by consuming its upper low liability indexed grain(s). For grain #9, its orientation changes from {101} to ~ {212} orientation, which is an 11.7° rotation. These grains are bound by both HAGBs and a LAGB after cyclic loading.

Fig. 7(a) and (b) are the IPF texture maps of the Cu grains in both the top and bottom layers for the pre-tested and post-20,000 cycle fatigued multilayers. As done above, in the supplementary section of this paper, the specific pole figures for each orientation for each location in the composite is provided. Before fatigue testing, a weak {001}-{112}, {101}, and {111} textures are observed, Fig. 7(a); in comparison, the post-tested Cu layers show a much stronger {101} texture and weaker {001}, {112} and {101} orientations, Fig. 7(b). The previous {111} texture was relatively constant. Fig. 7(c) and (d) are the IPF texture maps of the nanocrystalline Cu grains in the top layer, which is closer to the indenter as compared to the bottom Cu layer. For this layer, high cycle fatigue did not induce a severe IPF texture evolution. The previous {001}, {112}, and {111}-{101} textures still exist, Fig. 7(c), while some specific texture's intensity evolved after cyclic loading. A stronger {101} texture and a weaker {112} texture are shown, Fig. 7(d). The IPF texture maps of the Cu grains in bottom layer in the pre- and post-tested states, Fig. 7(e) and (f). Under the non-deformed condition, the bottom Cu layer existed a weak {111} and {101} texture and a strong {001}-{112}-{102} texture. After fatigue testing, modest development of {111} texture was now detected while strong {001}-{112}-{102} texture changed to {102}-{101} texture. Such overall and individual texture changes further confirmed the Cu grain rotation in both top and bottom layers under cyclic loading.

The grain size of the multilayer pre- and post-fatigue testing are plotted in Fig. 8. The mean grain size in the pre- and post-tested states were 37 ± 11 nm and 31 ± 9 nm, respectively. Though the mean size has been slightly reduced (analyzing the same area), the change is within the standard deviation. Furthermore, the grain size distribution is about the same, with the pre-tested sample showing a notable larger grain sizes in the 70 nm and 80 nm binned groupings, Fig. 8(a). Similarly, the grain size histogram for the top Cu layer is plotted in Fig. 8(b) with a pre- and post-mean grain size of 35 ± 11 nm and 31 ± 9 nm, respectively. Here the mean sizes are nearly identical and the distribution of the grain sizes are apparent. For the bottom Cu layer, the average grain sizes are 40 ± 12 nm and 32 ± 9 nm under pre- and post-testing conditions, respectively. The previously mentioned large grain is found in the bottom layer, between 70 and 80 nm, Fig. 8(c). Thus, the high cyclic fatigue, at this loading condition, did not induce a noticeable grain growth in the multilayer, which differs from the prior monotonic loading behavior.

4. Discussion

With the application of the monotonic indentation, the two amorphous layers were not in contact with the indenter and did not show any notable diffraction contrast changes as compared to the upper most amorphous layer that was in direct contact with the indenter. These two layers also did not reveal any notable reduction in their relative thicknesses, indicative of elastic deformation. In contrast, the upper most amorphous layer had varied bright field contrast evident by a distinct dark band in the layer where the indenter pressed into the material, Fig. 1(g). The permanent deformation crater, coupled with the contrast variation, confirms that shear bands initiated and propagated through this layer. Since the other two amorphous layers do not reveal any notable changes, the Cu layers, and in particular to the top Cu layer, likely blunted and accommodated the propagation of the deformation through the structure. Besides the upper most amorphous layer, a noticeable thickness change was also observed in top Cu layer after unloading by comparing Fig. 1(f) and (g). During *in situ* indentation, this Cu layer experienced both elastic and plastic deformation. Though elastic recovery is well known and expected, in of itself it is insufficient to fully explain the nearly 12 nm change observed. By virtue of being nanocrystalline, significant plastic recovery can occur, which has been reported in other face centered cubic metals such as Al and Au after unloading [76,77]. Such reversible plasticity here explains the additional thickness recovery noted in this top nanocrystalline Cu layer.

Upon indenting to ~ 32 nm in depth, the load response was constant indicating a relatively stable deformation, or other words, no dominate dislocation propagation within the Cu grains that would create a jump or transition in load with further penetration, which was noted to be a response in a Cu (only) film undergoing similar indentation [51]. Rather these Cu grains, based on their sizes, rotated, as well as underwent limited grain growth, rather than heavily plastically deformed by the propagation of extensive dislocation activity within the grains. The grain rotation mechanism is supported by the ACOM characterization that detected individual grain orientations changed between pre- and post-testing, with invariant changes noted in some of the neighboring grains. These orientation changes were most dominate in this top Cu layer, Fig. 2. This is supported by the IPF texture evolution of top Cu layer where both orientation distribution and orientation intensity during indentation, Fig. 3(c) and (d), is plotted and compared to equivalent types of plots for the bottom Cu layer, where only changes in intensity were noted, Fig. 3(e) and (f). In addition to the Cu response, the lack of hardening may also have contributions from the localized deformation in the upper most amorphous layer where strain softening can occur in amorphous alloys [78]. These ideas will be further expanded upon in the forthcoming FE modeling.

Grain growth under indentation was noted in the Cu layers too, where such behavior has been reported in other materials under indentation [67,79]. Though the relative distribution in these grain sizes was approximately equivalent in the pre- and post-states, Fig. 4, the grain growth appears largely driven by existing larger grains in these distributions consuming the smaller grains that are in contact with them. This was highlighted by grain #3 in Fig. 2 which increased from ~ 95

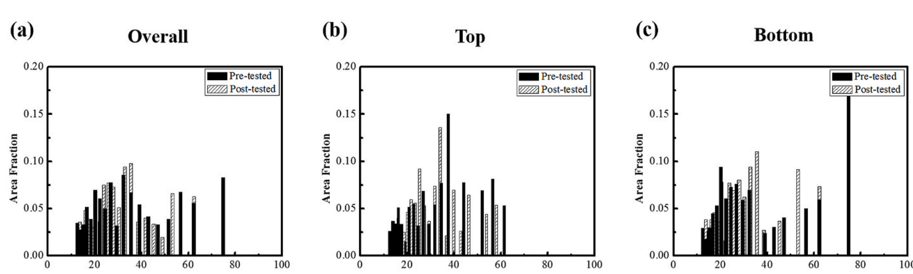

Fig. 8. The pre- and post- 20,000 cycles grain size histogram of **(a)** overall Cu layers **(b)** top Cu layer **(c)** bottom Cu layer.

nm to ~ 120 nm, with the loss of smaller grains in contact with it. This grain growth was also more apparent in the bottom Cu layer (from 39 ± 11 nm to 56 ± 16 nm) as compared to the top layer (29 ± 9 nm to 31 ± 10 nm). This would suggest that proximity to the indenter induced load has an effect on the deformation mechanism preference, either that be favoring rotation near the top layer and or grain growth in the bottom Cu layer.

To gain a deeper understanding of the stress/strain induced deformation, a FE simulation was performed based on the single loading indentation test and the results are shown in Fig. 9. The FE model replicates the *in situ* experimental setup but only considers the elastic and nominal elastic/micro-plastic deformation regions (i.e., to 32 nm indentation depth) without evoking complicated coupled deformation mechanisms in the multilayered composites [80]. The simulation result (red dashed line) is closely matched with the experimental one (black line), Fig. 9(a), and three critical moments, at displacements of 17 nm, 25 nm, and 32 nm, were identified before the indentation depth reaches its full plastic part.

The FE simulation reproduced load-displacement curve matches well to the experimental data in the elastic region right before the first critical moment at about 17 nm, Fig. 9(a). Based on the contrast changes in the bright field images taken at the displacement near 17 nm, as well as the modest shift in the experimental load-displacement curve, Fig. 1(a) or Fig. 9(a), it would suggest that the top Cu layer in the multilayer might be at yielding. The corresponding maximum shear stress field underneath the indenter overlaps the bright field image shown in Fig. 9(b). The maximum shear stress to initiate the yielding behavior of nanocrystalline Cu, about 0.82 GPa, is estimated, and is lower than the critical stress to initiate a shear band [81]. At about 25 nm indentation depth, a plastic deformation crater appears in the CuZr layer underneath the indenter in the simulation. As shown in Fig. 9(c), the stress is concentrated near the indentation site where the plastic deformation crater is located. The overlap, including both size and shape, between the high-stress concentration region in the FE model and the plastic crater in the bright field TEM, Fig. 1, match closely. The maximum shear stress is about 5.2 GPa in the vicinity of the crater, close to the value that triggers the shear transformation zone [82]. This behavior also confirms shear-dictated stress relaxation mechanisms.

The last critical moment occurs at about 32 nm indentation depth, and a large pop-in event on the experimental load-displacement curve appears, Fig. 1(a) or Fig. 9(a), as well as significant shear stresses in the top most amorphous layer in the simulation, Fig. 9(d). This pop-in event is largely caused by the formation of catastrophic shear bands. Although shear bands may start forming in the $Cu_{45}Zr_{55}$ layer, even before 17 nm indentation depth, their effects are mitigated by the deformed Cu layer until the penetration activates dislocation nucleation at the interface between two layers and one or more slip system(s) activate [83]. Due to the geometry, the Hertzian contact model is not suitable for this particular study [84]. Therefore, it is difficult to estimate the trajectory of the shear bands accurately. Nevertheless, as shown in Fig. 1(b)–(d), we can still attempt to apply the slip line analysis to achieve a rough estimate [16]. In this case, the critical stress is about 1.85 GPa.

Though other works have used either atomistic modeling and/or high resolution TEM to capture atomic scale deformation responses created by indentation in C/A layers [22,35,83], at this field of view, a loss in characterizing the slightly lower length scale (tens to hundreds of nanometers) can be lost. Through the coupling of FE and ACOM methods, we are able to capture this length scale and quantify the overall microstructure response created by the co-deformation. Through the use of ACOM, we have been able to track which specific grains rotated and by how much. Such information would be difficult, if not impossible, to determine from contrast changes in the bright field images. It should be noted that ACOM is a technique based on crystalline diffraction; therefore, it can only be used for assessing the crystalline layers in the C/A nanolaminate. By using the FE modeling, we are then able to quantitatively ascertain the deformation behavior. The in-plane displacement vectors from our modeling, Fig. 9(e), provide a clear indication of how (i.e., the mechanism) for grain rotation measured by

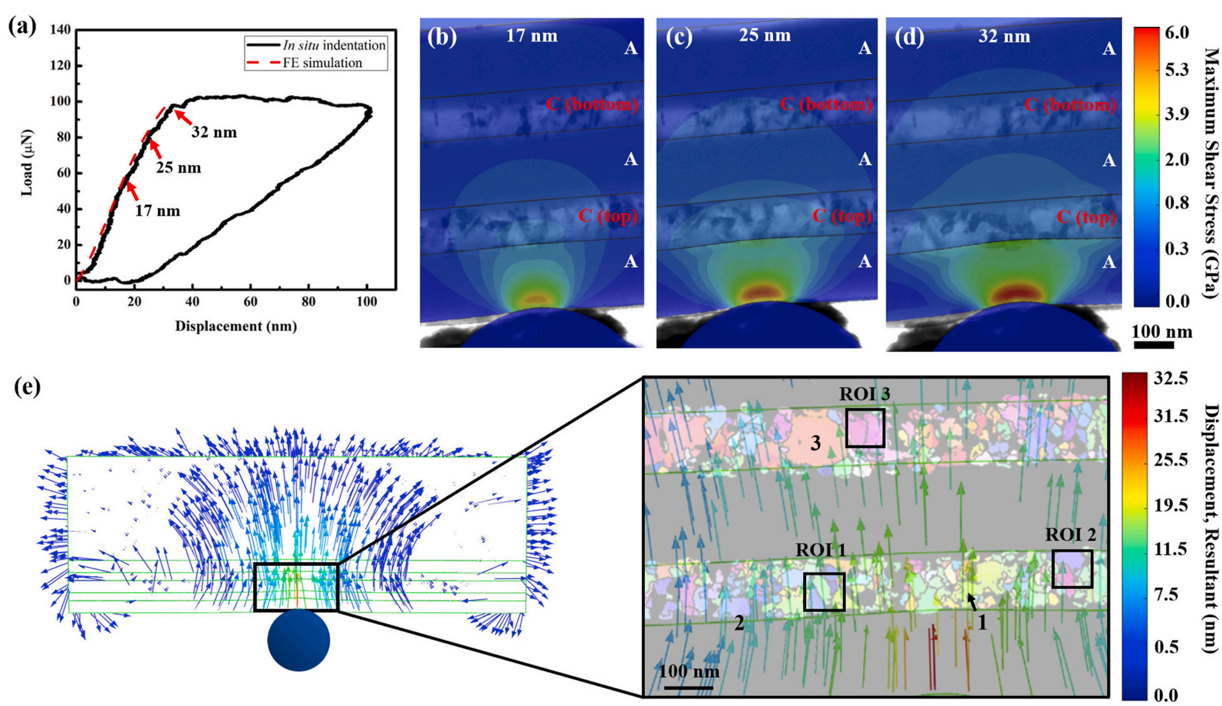

Fig. 9. (a) Experimental (solid black line) and simulated (dashed red line) load-displacement curves of Cu 105 nm/$Cu_{45}Zr_{55}$ 160 nm multilayer under *in situ* indentation with three critical displacements selected. Overlapped FE simulated maximum shear stress map and TEM bright field image at **(b)** 17 nm **(c)** 25 nm and **(d)** 32 nm displacement during indentation. **(e)** In-plane displacement vector field of the whole FE model at 32 nm displacement during indentation (left) with the selected main deformation region magnified (right) and overlapped with the post-indented ACOM grain orientation data of Cu layers shown in Fig. 2(b). (For interpretation of the references to color in this figure legend, the reader is referred to the Web version of this article.)

the ACOM measurements. As shown in Fig. 2 some grains (such as #4, #7, #8, #9) did not rotate while other grains (such as #1, #5, and #6) changed orientation between the pre- and post-deformation experiments. These grains are both in and away from the direct deformation region. These collective findings of some but not all grains rotating would support that the film did not undergo significant rigid body rotation; if it had, then all of these grains would have related changes in orientation associated with the bending. In a recent paper by some of the authors here [51], ACOM can quantify the extent of foil bending by a gradient change in the grain texture, which was not observed to occur in this multilayer foil. Furthermore, the rotation of the grains are well below the C/A interface, where the transmission of a shear zone from amorphous layers would be unlikely. Thus, any effect of the shear bands on rotation is negligible on the observed behavior, by virtue of them being explained by the modeled displacement vectors.

With specific grains rotating, we employed the FE simulation to elucidate the specificity of these rotations. The in-plane displacement vector field imposed by the indenter in our simulations was directly laid over the experimental ACOM post-indented sample map, Fig. 9(e). Grains #1, #5 (in ROI 1), and #6 (in ROI 2) in Fig. 2 are located in a rotated displacement vector field near the indentation site, Fig. 9(e). As a result, after indentation, grains #1, #5, and #6 rotated, based on the ACOM orientation maps in Fig. 2. As previously noted in the results, grain #1 rotates in a clockwise motion (16.8°) between the pre- and post- orientation and would follow the displacement-field vector-path, i.e. a clockwise rotation. Grain #3 is located in a near vertical displacement vector field underneath the indentation site. As a result, it did not suffer a noticeable grain rotation during indentation. For the un-rotated grains that resided in a displacement vector field that would suggest rotation, most of them (like grains #2, #4 (in ROI 1), and #7 (in ROI 2)) have the ~ {111} orientation, Fig. 2, which is the slip plane orientation for a face center cubic crystal. When the indenting force is applied on these crystalline layers that are parallel to the {111} slip planes, they would most likely prefer to accommodate the deformation by changing their shapes (plastic deformation) rather than rotating. The strain tensor mismatch from grain-to-grain, grain boundary compliance, as well as the interface compliance will also affect the grain rotation. Nevertheless, the clockwise and counterclockwise rotation of specific grains in the Cu layers observed here follows the path of the overall trend for the in-plane displacement vectors, Fig. 9(e), indicating the in-plane displacement contribution to the Cu grain rotation. By directly combining the simulated stress field to the ACOM results, the ability to understand the rotation of specific grains became more apparent.

It is noteworthy that the ability for the grains to rotate is likely assisted by their access to a free surface inherent to the TEM thin foil. In contrast, in a bulk sample, where all of its neighboring grains encase a specific grain, rotation would be more difficult. Thus, restraint should be used in generally applying the prevalence of the rotation mechanism as a general response.

With the single loading experiments discussed, we now address the cyclic loading behavior. The very modest plastic deformation crater for the fatigued tapped multilayer is contributed to the lower tapping load of 20 ± 5 μN (compared to the single indent load that, at completion of the indent, was ~ 100 μN). This load was well within the elastic and nominal elastic/micro-plastic deformation region modeled above, Fig. 9 (a). This would suggest that fewer STZs in the amorphous layer(s) would be triggered during cyclic loading and those nucleated and propagated would be easily absorb by the C/A interface [16,39]. This enabled the other amorphous layers, similar to the single loading experiment, to undergo elastic deformation. In addition, the higher hardness of the amorphous $Cu_{45}Zr_{55}$, ~6.1 GPa, as compared to that of the Cu, ~1.8 GPa, facilitated the deformation to be largely accommodated by the 'softer' Cu [16,85,86]. The response of the two Cu layers under the cyclic loading was similar to each other and noted to be dominated by grain rotation noted by global texture evolution, Fig. 7, and not grain growth, Fig. 8, or other obvious plastic mechanisms. The grains generally evolved towards a {101} texture for orientations, while also maintaining a relative invariance between the pre- and post-cyclic indents for {111}, Fig. 7. The invariance of the {111} is contributed to it being a preferred slip orientation for Cu. Interestingly, the single indent revealed a similar preference for {101} in the top layer with deformation, Fig. 3(c)–(d), whereas the bottom layer revealed a decrease in {101}with deformation, Fig. 3(e)–(f). Since the single indent top Cu layer, Fig. 3(c)–(d), and the cyclic testing for both layers, Fig. 7(c)–(f), had minimal deformation induced grain growth, it would suggest that a grain rotation towards {101} is preferred. The decrease in the {101} for the bottom Cu layer in the single indent, Fig. 3(f), is contributed to those grains being consumed by the more prevalent grain growth mechanism, as seen in ROI 3 in Fig. 2(g)–(h) where grain #10's green {101} is consumed leaving grains #8 and #9, which have the reddish-pink hue ~ {112} orientation, in its former place. In prior work on a purely nanocrystalline Cu foil, grain growth was noted to be much more prevalent under high cycle loading [50]. This difference in the Cu response is contributed to the nanocrystalline layers being both confined in geometry and shielded from direct contact with the indenter. The load to the nanocrystalline Cu layers was dissipated by the presence of the high hardness amorphous layer(s) above it.

If grain rotation is the preferred deformation mechanism, and facilitated by the TEM foil geometry, it suggests that these nanolaminate composites may have sufficient survivability to retain small crystallite sizes for strength and not undergo catastrophic STZ failures in applications where repeated contact occurs within the applied conditions studied. These suggest future opportunities of investigation of these materials as coatings on bulk components.

5. Conclusion

In this present study, the monotonic indentation and cyclic deformation responses in a nanocrystalline/amorphous $Cu/Cu_{45}Zr_{55}$ nanolaminate multilayer were investigated via *in situ* TEM, where the Cu layer thickness was 105 nm and the $Cu_{45}Zr_{55}$ was 160 nm. The single loading was done to a depth of 100 nm whereas the high cycle fatigue test was done up to 20,000 cycles. This is the first time that the C/A nanolaminate was *in situ* tested under cyclic loading with the microstructure evolutions, such as the grain orientation and grain size, quantified using ACOM mapping.

Upon single indentation, contrast changes were observed in the upper most amorphous layer that was in direct contact with the indenter, whereas the other amorphous layers in between the two Cu layers revealed no changes in thickness or contrast. The Cu grains within the layers exhibited diffraction contrast during loading, suggestive of grain rotation as a deformation mechanism. Using ACOM measurements prior to and after the indent, specific grains were noted to rotate while others did not rotate with these observations varying across the TEM foil with respect to the indent contact point. ACOM has provided an unambiguous determination of this rotation that could only be inferred from contrast changes in the bright field. This grain rotation was particularly evident in the upper most Cu layer just under the amorphous layer that was in direct contact with the indenter. The lack of bend contouring of the foil during testing, and more specifically the retention of specific neighboring grains' texture while others changed, suggested this mechanism to be grain specific. Using a FE model of the displacement vectors, and the known grain orientation prior to loading, changes in grain orientation were explained in relationship to the stress flow pattern. The ability for the grains to rotate was enhanced by their access to the free surface.

Besides grain rotation, mechanically induced grain growth was observed in the bottom Cu layer for the single indent investigation. This grain growth was dominated by larger grains consuming smaller grains as well as resulting in overall specific orientation changes in the multilayer.

Using FE modeling, we were able to note particular indent depths in the elastic/micro-plastic deformation regime that corresponded well to the experimental changes in the load-displacement slope. These include a stress field that was below the critical stress to nucleate a shear band but was at the yield stress for Cu; the onset of a permanent crater into the top amorphous layer; and the clear onset of shear transformation zones with an evident 'pop-in' event.

For the high cycle fatigue indent test, the global texture of the film evolved towards {101}, unless an existing {111} orientation was present with the grain orientation evolution. Grain rotation was noted in both Cu layers, with a lack of strong evidence for deformation induced grain growth in either layer. The mean grain size and grain size distribution remained relatively equivalent between the pre- and post-fatigue indented ACOM analysis. As the tapping load (20 ± 5 μN) was within the linear portion of the load-displacement curve (elastic/micro-plastic deformation region), a minimal plastic crater formed on the outer amorphous film surface that contacted the indenter. This was indicative that a lower number of STZ occurred in the amorphous phase, with the deformation accommodation dominated largely by the grain rotation in the two Cu layers and an overall texture orientation towards {101}, unless the grains were already in a {111} orientation, which remained between the pre- and post-cycling analysis. The invariance of this close packed orientation is explained by it being a preferred slip orientation for Cu.

Data availability statement

The raw/processed data required to reproduce these findings cannot be shared at this time as the data also forms part of ongoing studies. Data will be made available on request once the ongoing studies have been done.

CRediT authorship contribution statement

Qianying Guo: Investigation, Formal analysis, Conceptualization, Methodology, Writing - original draft. **Yucong Gu:** Investigation, Formal analysis, Validation, Software, Writing - original draft. **Christopher M. Barr:** Validation. **Thomas Koenig:** Investigation. **Khalid Hattar:** Validation, Writing - review & editing. **Lin Li:** Validation, Writing - review & editing, Supervision. **Gregory B. Thompson:** Formal analysis, Conceptualization, Writing - review & editing, Supervision, Funding acquisition, Project administration.

Declaration of competing interest

The authors declare that they have no known competing financial interests or personal relationships that could have appeared to influence the work reported in this paper.

Acknowledgement

The QG, TK, and GBT acknowledge the support of NSF-DMR-1207220. YC and LL acknowledges the support from NSF-CMMI-1727875. A portion of this manuscript was conducted in Center for Nanophase Materials Sciences (QG) by PD Educational Investment. The Bruker PI-95 indenter was acquired through the NSF-DMR-1531722. C. M.B. and K.H. time was fully supported by the Division of Materials Science and Engineering, Office of Basic Energy Sciences, U.S. Department of Energy. This work was performed, in part, at the Center for Integrated Nanotechnologies, an Office of Science User Facility operated for the U.S. Department of Energy (DOE) Office of Science. Sandia National Laboratories is a multimission laboratory managed and operated by National Technology & Engineering Solutions of Sandia, LLC, a wholly owned subsidiary of Honeywell International, Inc., for the U.S. DOE's National Nuclear Security Administration under contract DE-NA-0003525. The views expressed in the article do not necessarily represent the views of the U.S. DOE or the United States Government.

Appendix A. Supplementary data

Supplementary data to this article can be found online at https://doi.org/10.1016/j.msea.2020.140074.

References

[1] S. Veprek, S. Reiprich, A concept for the design of novel superhard coatings, Thin Solid Films 268 (1) (1995) 64–71.
[2] S. Veprek, M. Haussmann, S. Reiprich, Superhard nanocrystalline W2N/amorphous Si3N4 composite materials, J. Vac. Sci. Technol. 14 (1) (1996) 46–51.
[3] C.A. Schuh, T.C. Hufnagel, U. Ramamurty, Mechanical behavior of amorphous alloys, Acta Mater. 55 (12) (2007) 4067–4109.
[4] Z. Zhang, J. Eckert, L. Schultz, Fatigue and fracture behavior of bulk metallic glass, MMTA 35 (11) (2004) 3489–3498.
[5] S.J. Pang, T. Zhang, K. Asami, A. Inoue, Synthesis of Fe–Cr–Mo–C–B–P bulk metallic glasses with high corrosion resistance, Acta Mater. 50 (3) (2002) 489–497.
[6] C. Gilbert, R. Ritchie, W. Johnson, Fracture toughness and fatigue-crack propagation in a Zr–Ti–Ni–Cu–Be bulk metallic glass, Appl. Phys. Lett. 71 (4) (1997) 476–478.
[7] G. He, W. Löser, J. Eckert, Microstructure and mechanical properties of the Zr66.4Cu10.5Ni8.7Al8Ta6.4 metallic glass-forming alloy, Scripta Mater. 48 (11) (2003) 1531–1536.
[8] A.S. Argon, Plastic deformation in metallic glasses, Acta Metall. 27 (1) (1979) 47–58.
[9] D. Pan, A. Inoue, T. Sakurai, M. Chen, Experimental characterization of shear transformation zones for plastic flow of bulk metallic glasses, Proc. Natl. Acad. Sci. Unit. States Am. 105 (39) (2008) 14769–14772.
[10] E.R. Homer, C.A. Schuh, Mesoscale modeling of amorphous metals by shear transformation zone dynamics, Acta Mater. 57 (9) (2009) 2823–2833.
[11] S.X. Song, X.L. Wang, T.G. Nieh, Capturing shear band propagation in a Zr-based metallic glass using a high-speed camera, Scripta Mater. 62 (11) (2010) 847–850.
[12] D.C. Hofmann, J.-Y. Suh, A. Wiest, G. Duan, M.-L. Lind, M.D. Demetriou, W. L. Johnson, Designing metallic glass matrix composites with high toughness and tensile ductility, Nature 451 (7182) (2008) 1085–1089.
[13] M.E. Launey, D.C. Hofmann, W.L. Johnson, R.O. Ritchie, Solution to the problem of the poor cyclic fatigue resistance of bulk metallic glasses, Proc. Natl. Acad. Sci. Unit. States Am. 106 (13) (2009) 4986–4991.
[14] P. Yu, K.B. Kim, J. Das, F. Baier, W. Xu, J. Eckert, Fabrication and mechanical properties of Ni–Nb metallic glass particle-reinforced Al-based metal matrix composite, Scripta Mater. 54 (8) (2006) 1445–1450.
[15] J. Eckert, A. Kübler, L. Schultz, Mechanically alloyed Zr 55 Al 10 Cu 30 Ni 5 metallic glass composites containing nanocrystalline W particles, J. Appl. Phys. 85 (10) (1999) 7112–7119.
[16] C. Sterwerf, T. Kaub, C. Deng, G.B. Thompson, L. Li, Deformation mode transitions in amorphous-Cu45Zr55/crystalline-Cu multilayers, Thin Solid Films 626 (2017) 184–189.
[17] T.C. Hufnagel, C.A. Schuh, M.L. Falk, Deformation of metallic glasses: recent developments in theory, simulations, and experiments, Acta Mater. 109 (2016) 375–393.
[18] T. Phan, J. Rigelesaiyin, Y. Chen, A. Bastawros, L. Xiong, Metallic glass instability induced by the continuous dislocation absorption at an amorphous/crystalline interface, Acta Mater. 189 (2020) 10–24.
[19] Y. Wang, J. Li, A.V. Hamza, T.W. Barbee, Ductile crystalline–amorphous nanolaminates, Proc. Natl. Acad. Sci. Unit. States Am. 104 (27) (2007) 11155–11160.
[20] B. Cheng, J.R. Trelewicz, Mechanistic coupling of dislocation and shear transformation zone plasticity in crystalline-amorphous nanolaminates, Acta Mater. 117 (2016) 293–305.
[21] C. Brandl, T.C. Germann, A. Misra, Structure and shear deformation of metallic crystalline–amorphous interfaces, Acta Mater. 61 (10) (2013) 3600–3611.
[22] Z. Pan, T.J. Rupert, Amorphous intergranular films as toughening structural features, Acta Mater. 89 (2015) 205–214.
[23] H. Song, J. Xu, Y. Zhang, S. Li, D. Wang, Y. Li, Molecular dynamics study of deformation behavior of crystalline Cu/amorphous Cu50Zr50 nanolaminates, Mater. Des. 127 (2017) 173–182.
[24] Y. Cui, Y. Shibutani, S. Li, P. Huang, F. Wang, Plastic deformation behaviors of amorphous-Cu50Zr50/crystalline-Cu nanolaminated structures by molecular dynamics simulations, J. Alloys Compd. 693 (2017) 285–290.
[25] E. Alishahi, C. Deng, Orientation dependent plasticity of metallic amorphous-crystalline interface, Comput. Mater. Sci. 141 (2018) 375–387.
[26] X. Zhou, C. Chen, Molecular dynamic simulations of the mechanical properties of crystalline/crystalline and crystalline/amorphous nanolayered pillars, Comput. Mater. Sci. 101 (2015) 194–200.
[27] H. Song, J. Xu, Q. Deng, Y. Li, Effect of interface structure on deformation behavior of crystalline Cu/amorphous CuZr sandwich structures, Phys. Lett. 383 (2–3) (2019) 215–220.
[28] G.B. Thompson, R. Banerjee, H.L. Fraser, Predicting pseudomorphic phases in multilayers: hexagonal-closed-packed Nb in Nb/Zr, Appl. Phys. Lett. 84 (7) (2004) 1082–1084.
[29] G.B. Thompson, R. Banerjee, S.A. Dregia, H.L. Fraser, Phase stability of bcc Zr in Nb/Zr thin film multilayers, Acta Mater. 51 (18) (2003) 5285–5294.

[30] Q. Guo, L. Wan, X.-x. Yu, F. Vogel, G.B. Thompson, Influence of phase stability on the in situ growth stresses in Cu/Nb multilayered films, Acta Mater. 132 (2017) 149–161.
[31] Q. Guo, G.B. Thompson, Evolution of in situ growth stresses and interfacial structure in phase changing Cu/V multilayered thin films, Acta Mater. 148 (2018) 63–71.
[32] H.P.A. Ali, A. Budiman, Advances in in situ microfracture experimentation techniques: a case of nanoscale metal–metal multilayered materials, J. Mater. Res. 34 (9) (2019) 1449–1468.
[33] S. Li, L. Pastewka, P. Gumbsch, Glass formation by severe plastic deformation of crystalline Cu| Zr nano-layers, Acta Mater. 165 (2019) 577–586.
[34] Y. Wang, R. Fritz, D. Kiener, J. Zhang, G. Liu, O. Kolednik, R. Pippan, J. Sun, Fracture behavior and deformation mechanisms in nanolaminated crystalline/amorphous micro-cantilevers, Acta Mater. 180 (2019) 73–83.
[35] Y. Cui, O.T. Abad, F. Wang, P. Huang, T.-J. Lu, K.-W. Xu, J. Wang, Plastic deformation modes of CuZr/Cu multilayers, Sci. Rep. 6 (2016), 23306.
[36] J.Y. Kim, D. Jang, J.R. Greer, Nanolaminates utilizing size-dependent homogeneous plasticity of metallic glasses, Adv. Funct. Mater. 21 (23) (2011) 4550–4554.
[37] H. Chou, X. Du, C. Lee, J. Huang, Enhanced mechanical properties of multilayered micropillars of amorphous ZrCuTi and nanocrystalline Ta layers, Intermetallics 19 (7) (2011) 1047–1051.
[38] I. Knorr, N. Cordero, E.T. Lilleodden, C.A. Volkert, Mechanical behavior of nanoscale Cu/PdSi multilayers, Acta Mater. 61 (13) (2013) 4984–4995.
[39] W. Guo, E. Jägle, J. Yao, V. Maier, S. Korte-Kerzel, J.M. Schneider, D. Raabe, Intrinsic and extrinsic size effects in the deformation of amorphous CuZr/nanocrystalline Cu nanolaminates, Acta Mater. 80 (2014) 94–106.
[40] M. Liu, X. Du, I. Lin, H. Pei, J. Huang, Superplastic-like deformation in metallic amorphous/crystalline nanolayered micropillars, Intermetallics 30 (2012) 30–34.
[41] M. Liu, J. Huang, H. Chou, Y. Lai, C. Lee, T. Nieh, A nanoscaled underlayer confinement approach for achieving extraordinarily plastic amorphous thin film, Scripta Mater. 61 (8) (2009) 840–843.
[42] A. Avilov, K. Kuligin, S. Nicolopoulos, M. Nickolskiy, K. Boulahya, J. Portillo, G. Lepeshov, B. Sobolev, J.P. Collette, N. Martin, A.C. Robins, P. Fischione, Precession technique and electron diffractometry as new tools for crystal structure analysis and chemical bonding determination, Ultramicroscopy 107 (6) (2007) 431–444.
[43] P. Moeck, S. Rouvimov, E. Rauch, M. Véron, H. Kirmse, I. Häusler, W. Neumann, D. Bultreys, Y. Maniette, S. Nicolopoulos, High spatial resolution semi-automatic crystallite orientation and phase mapping of nanocrystals in transmission electron microscopes, Cryst. Res. Technol. 46 (6) (2011) 589–606.
[44] E. Rauch, M. Véron, Automated crystal orientation and phase mapping in TEM, Mater. Char. 98 (2014) 1–9.
[45] J.G. Brons, G.B. Thompson, Orientation mapping via precession-enhanced electron diffraction and its applications in materials science, JOM 66 (1) (2014) 165–170.
[46] I. Ghamarian, Y. Liu, P. Samimi, P.C. Collins, Development and application of a novel precession electron diffraction technique to quantify and map deformation structures in highly deformed materials—as applied to ultrafine-grained titanium, Acta Mater. 79 (2014) 203–215.
[47] P.K. Suri, J.E. Nathaniel, C.M. Barr, J.K. Baldwin, K. Hattar, M.L. Taheri, Defect characterization in irradiated nanocrystalline materials via automated crystal orientation mapping, Microsc. Microanal. 23 (S1) (2017) 2236–2237.
[48] J. Roqué Rosell, J. Portillo Serra, T. Aiglsperger, S. Plana-Ruiz, T. Trifonov, J. A. Proenza, Au crystal growth on natural occurring Au—Ag aggregate elucidated by means of precession electron diffraction (PED), J. Cryst. Growth 483 (2018) 228–235.
[49] I. Ghamarian, P. Samimi, G.S. Rohrer, P.C. Collins, Determination of the five parameter grain boundary character distribution of nanocrystalline alpha-zirconium thin films using transmission electron microscopy, Acta Mater. 130 (2017) 164–176.
[50] D.C. Bufford, D. Stauffer, W.M. Mook, S. Syed Asif, B.L. Boyce, K. Hattar, High cycle fatigue in the transmission electron microscope, Nano Lett. 16 (8) (2016) 4946–4953.
[51] Q. Guo, G.B. Thompson, In-situ indentation and correlated precession electron diffraction analysis of a polycrystalline Cu thin film, JOM 70 (7) (2018) 1081–1087.
[52] A. Kobler, A. Kashiwar, H. Hahn, C. Kübel, Combination of in situ straining and ACOM TEM: a novel method for analysis of plastic deformation of nanocrystalline metals, Ultramicroscopy 128 (2013) 68–81.
[53] F. Mompiou, M. Legros, Quantitative grain growth and rotation probed by in-situ TEM straining and orientation mapping in small grained Al thin films, Scripta Mater. 99 (2015) 5–8.
[54] A. Inoue, Bulk amorphous and nanocrystalline alloys with high functional properties, Mater. Sci. Eng: A 304–306 (2001) 1–10.
[55] M.J. Cordill, C.R. Weinberger, Mechanical behavior at the nanoscale: what's in your toolbox? JOM (2018) 1–3.
[56] J.D. Schuler, C.M. Barr, N.M. Heckman, G. Copeland, B.L. Boyce, K. Hattar, T. J. Rupert, In situ high-cycle fatigue reveals importance of grain boundary structure in nanocrystalline Cu-Zr, JOM (2018) 1–12.
[57] Q. Guo, Y.S. Chun, J.H. Lee, Y.-U. Heo, C.S. Lee, Enhanced low-cycle fatigue life by pre-straining in an Fe-17Mn-0.8 C twinning induced plasticity steel, Met. Mater. Int. 20 (6) (2014) 1043–1051.
[58] A. Minor, E. Lilleodden, E. Stach, J. Morris, Direct observations of incipient plasticity during nanoindentation of Al, J. Mater. Res. 19 (2004) 176–182, 01.
[59] L.A. Giannuzzi, F.A. Stevie, A review of focused ion beam milling techniques for TEM specimen preparation, Micron 30 (3) (1999) 197–204.
[60] G.B. Thompson, M.K. Miller, H.L. Fraser, Some aspects of atom probe specimen preparation and analysis of thin film materials, Ultramicroscopy 100 (1–2) (2004) 25–34.
[61] K. Thompson, D. Lawrence, D.J. Larson, J.D. Olson, T.F. Kelly, B. Gorman, In situ site-specific specimen preparation for atom probe tomography, Ultramicroscopy 107 (2–3) (2007) 131–139.
[62] P.J. Felfer, T. Alam, S.P. Ringer, J.M. Cairney, A reproducible method for damage-free site-specific preparation of atom probe tips from interfaces, Microsc. Res. Tech. 75 (4) (2012) 484–491.
[63] J. Ciston, B. Deng, L. Marks, C. Own, W. Sinkler, A quantitative analysis of the cone-angle dependence in precession electron diffraction, Ultramicroscopy 108 (6) (2008) 514–522.
[64] A. Morawiec, E. Bouzy, On the reliability of fully automatic indexing of electron diffraction patterns obtained in a transmission electron microscope, J. Appl. Crystallogr. 39 (1) (2006) 101–103.
[65] D. Viladot, M. Véron, M. Gemmi, F. Peiró, J. Portillo, S. Estradé, J. Mendoza, N. Llorca-Isern, S. Nicolopoulos, Orientation and phase mapping in the transmission electron microscope using precession-assisted diffraction spot recognition: state-of-the-art results, J. Microscopy 252 (1) (2013) 23–34.
[66] E.F. Rauch, L. Dupuy, Comments onOn the reliability of fully automatic indexing of electron diffraction patterns obtained in a transmission electron microscope'by Morawiec & Bouzy, Applied Crystallography 39 (1) (2006) 104–105, 2006.
[67] J.G. Brons, J.A. Hardwick, H.A. Padilla, K. Hattar, G.B. Thompson, B.L. Boyce, The role of copper twin boundaries in cryogenic indentation-induced grain growth, Mater. Sci. Eng: A 592 (2014) 182–188.
[68] N. Wang, F. Yan, L. Li, Mesoscopic examination of cyclic hardening in metallic glass, J. Non-Cryst. Solids 428 (Supplement C) (2015) 146–150.
[69] P. Liu, S.C. Mao, L.H. Wang, X.D. Han, Z. Zhang, Direct dynamic atomic mechanisms of strain-induced grain rotation in nanocrystalline, textured, columnar-structured thin gold films, Scripta Mater. 64 (4) (2011) 343–346.
[70] M. Jin, A.M. Minor, E.A. Stach, J.W. Morris, Direct observation of deformation-induced grain growth during the nanoindentation of ultrafine-grained Al at room temperature, Acta Mater. 52 (18) (2004) 5381–5387.
[71] M.-R. He, S.K. Samudrala, G. Kim, P.J. Felfer, A.J. Breen, J.M. Cairney, D. S. Gianola, Linking stress-driven microstructural evolution in nanocrystalline aluminium with grain boundary doping of oxygen, Nat. Commun. 7 (2016), 11225.
[72] T. Rupert, D. Gianola, Y. Gan, K. Hemker, Experimental observations of stress-driven grain boundary migration, Science 326 (5960) (2009) 1686–1690.
[73] R.J. Asaro, S. Suresh, Mechanistic models for the activation volume and rate sensitivity in metals with nanocrystalline grains and nano-scale twins, Acta Mater. 53 (12) (2005) 3369–3382.
[74] K. Lu, L. Lu, S. Suresh, Strengthening materials by engineering coherent internal boundaries at the nanoscale, Science 324 (5925) (2009) 349–352.
[75] R. Sandström, On recovery of dislocations in subgrains and subgrain coalescence, Acta Metall. 25 (8) (1977) 897–904.
[76] J. Rajagopalan, J.H. Han, M.T.A. Saif, Plastic deformation recovery in freestanding nanocrystalline aluminum and gold thin films, Science 315 (5820) (2007) 1831–1834.
[77] J. Rajagopalan, C. Rentenberger, H.P. Karnthaler, G. Dehm, M.T.A. Saif, In situ TEM study of microplasticity and Bauschinger effect in nanocrystalline metals, Acta Mater. 58 (14) (2010) 4772–4782.
[78] H. Bei, S. Xie, E.P. George, Softening caused by profuse shear banding in a bulk metallic glass, Phys. Rev. Lett. 96 (10) (2006) 105503.
[79] D.S. Gianola, S. Van Petegem, M. Legros, S. Brandstetter, H. Van Swygenhoven, K. J. Hemker, Stress-assisted discontinuous grain growth and its effect on the deformation behavior of nanocrystalline aluminum thin films, Acta Mater. 54 (8) (2006) 2253–2263.
[80] W. Guo, B. Gan, J.M. Molina-Aldareguia, J.D. Poplawsky, D. Raabe, Structure and dynamics of shear bands in amorphous–crystalline nanolaminates, Scripta Mater. 110 (2016) 28–32.
[81] C. Packard, C. Schuh, Initiation of shear bands near a stress concentration in metallic glass, Acta Mater. 55 (16) (2007) 5348–5358.
[82] C.-C. Wang, J. Ding, Y.-Q. Cheng, J.-C. Wan, L. Tian, J. Sun, Z.-W. Shan, J. Li, E. Ma, Sample size matters for Al88Fe7Gd5 metallic glass: smaller is stronger, Acta Mater. 60 (13–14) (2012) 5370–5379.
[83] W. Guo, E.A. Jägle, P.-P. Choi, J. Yao, A. Kostka, J.M. Schneider, D. Raabe, Shear-induced mixing governs codeformation of crystalline-amorphous nanolaminates, Phys. Rev. Lett. 113 (3) (2014), 035501.
[84] K.L. Johnson, K.L. Johnson, Contact Mechanics, Cambridge university press, 1987.
[85] J.Y. Zhang, G. Liu, S.Y. Lei, J.J. Niu, J. Sun, Transition from homogeneous-like to shear-band deformation in nanolayered crystalline Cu/amorphous Cu–Zr micropillars: intrinsic vs. extrinsic size effect, Acta Mater. 60 (20) (2012) 7183–7196.
[86] A. Misra, J.P. Hirth, R.G. Hoagland, Length-scale-dependent deformation mechanisms in incoherent metallic multilayered composites, Acta Mater. 53 (18) (2005) 4817–4824.